

Microstructure Evolution of a Platinum-Modified Nickel-Aluminide Coating During Thermal and Thermo-mechanical Fatigue



PIERRE SALLOT, VINCENT MAUREL, LUC RÉMY, FRANCK N'GUYEN,
and ARNAUD LONGUET

The microstructure evolution of a platinum-modified nickel-aluminide coating on single-crystal nickel-based superalloy was investigated for various thermal cycling and thermo-mechanical fatigue (TMF) conditions in air for a long-term exposure. An increase in roughness and in $\beta \rightarrow \gamma'$ transformation rate depends similarly on maximum temperature, holding time at maximum temperature and applied stress. Moreover, the evolution of the interdiffusion zone (IDZ) is analyzed by making the distinction between two layers, according to the major phases observed within these layers, namely β -(Ni,Pt)Al and γ' -Ni₃Al. This distinction highlighted that the respective thickness evolution of these two layers are sensitive to each parameter of TMF tests with similar increase in evolution rate when increasing time, temperature, as well as applied stress. The distinctive features of phase transformation are finally discussed together with localization of phase transformation and measured evolution of phase transformation within the external coating and β - and γ' -IDZ layer thicknesses under thermal and thermo-mechanical fatigue. This analysis leads to a conclusion that grain boundaries within the external coating as well as interfaces, between thermally grown oxide, external coating, and IDZ, respectively, play a major role in diffusion, phase transformation, and microstructure evolution of typical platinum-modified nickel-aluminide coating.

DOI: 10.1007/s11661-015-2857-9

© The Minerals, Metals & Materials Society and ASM International 2015

I. INTRODUCTION

MATERIALS used to produce hot components of aero- and land-based gas turbine engines have to possess high strength, oxidation, and corrosion resistance, as they are subjected to different thermo-mechanical loadings at elevated temperatures close to 1373 K (1100 °C) and higher. Ni-based superalloys are particularly well designed to resist these severe conditions leading to high temperature creep. Nickel-aluminide and MCrAlY coatings are known to increase the oxidation resistance of the superalloys providing supplementary Al and/or Cr to form a stable α -Al₂O₃ (or Cr₂O₃) scale on the surface,^[1] which then protects the superalloy from further oxidation. Moreover, Pt is added to increase the adherence, as well as to decrease growth kinetics of the α -Al₂O₃ scale for nickel-aluminide coatings.^[2]

Platinum-modified nickel-aluminide coatings are produced through several stages: (i) Pt electroplating on the superalloy substrate, (ii) diffusion treatment under vacuum, followed by (iii) aluminization process.^[3] After such a procedure, the coating consists of either an external single-phase β -(Ni,Pt)Al layer or a dual-phase β -(Ni,Pt)Al + PtAl₂ layer depending on process parameters.^[3,4] Moreover, during the coating deposition the diffusion of elements from substrate to the external coating and vice versa leads to the formation of an interdiffusion zone (IDZ).^[3-6] Basuki *et al.*^[7] have also shown that for a typical nickel-aluminide coating deposited on René 80H, this IDZ was initially composed of a β -NiAl matrix that was progressively transformed into γ phase (nickel-based solid solution) during high temperature exposure.

Therefore, coating/substrate interdiffusion is an important phenomenon, as it affects coating microstructure and thus both oxidation resistance and mechanical properties of the substrate. For example, Nesbitt^[8] clearly illustrated the detrimental effect of diffusional degradations on the (Ni,Co)CrAl coating lifetime. In this case two mechanisms are responsible for coating degradation: Al loss due to the Al₂O₃ formation on the surface and Al loss due to the diffusion of Al from the coating to the superalloy substrate. Therefore, the coating becomes depleted in Al and is not able to supply enough Al to the surface for continuous growth of the Al₂O₃ scale, which finally leads to a catastrophic oxidation behavior. Such effects are observed as well for

PIERRE SALLOT, Advanced Materials R&D Engineer, is with Safran Tech, Rue Geneviève Aubé 78117, Chateaufort, France. Contact e-mail: pierre.sallot@safran.fr VINCENT MAUREL, Research Professor, LUC RÉMY, Senior Research Professor, and FRANCK N'GUYEN, Ph.D. Researcher, are with the PSL Research University, MAT - Centre des Matériaux, CNRS UMR 7633, MINES ParisTech, Evry Cedex, France. ARNAUD LONGUET, Material & Process Leader, is with Snecma, Rond Point René Ravaud, Réau, 77550, Moissy-Cramayel, France.

Manuscript submitted November 27, 2014.

Article published online April 7, 2015

both plain^[7,9,10] and Pt-modified nickel aluminide used as bond coats for typical thermal barrier coating (TBC).^[11–14]

Moreover, hot section components of aeroengines are subjected to both severe thermal gradients as well as to mechanical loads during the service. Thermo-mechanical fatigue (TMF) is thus a major issue for these parts, affecting both the Ni-based superalloy^[15–17] and the coating.^[9,18–21] For instance, it was shown that TMF strongly impacts life to spallation of TBC.^[22–26]

Nevertheless, the influence of TMF on microstructure stability of nickel-aluminide coating, when it is used without a protective ceramic layer, has been rarely reported. Some studies available in the literature are limited by relatively short-term exposure at high temperature,^[13,18,27,28] except several works where the loss in load bearing section^[29,30] and rafting of γ' -Ni₃Al precipitates^[17] are investigated.

Therefore, the current study aims to quantify the Pt-modified nickel-aluminide coating microstructure evolution during thermal cycling and TMF in air for long duration tests. Special attention is paid to the influence of maximum temperature, holding time at maximum temperature, and superimposed stress.

II. EXPERIMENTAL METHODOLOGY

A. Material

The substrate material used in the current study was the AM1 single-crystal nickel-based superalloy with the chemical composition given in Table I.

The deposition of platinum-modified nickel-aluminide coating on the superalloy consisted of several stages: (i) Pt electrodeposition (final Pt layer thickness less than 10 μm), followed by (ii) diffusion treatment under vacuum at 1323 K (1050 °C), and, finally, (iii) Al phase vapor deposition (APVS: aluminizing phase vapor sneema).^[31] After the described procedure the external coating consisted of β -(Ni,Pt)Al phase with the thickness of approximately 45 μm ; the interdiffusion zone was formed between the coating and the superalloy substrate and contained γ' phase and so-called topologically close-packed phases (tcp) enriched by W and Mo.

Thermal cycling and TMF tests were carried out directly on the samples after the coating deposition without any additional surface preparation.

B. Thermal Cycling and TMF Conditions

The coating microstructure evolution was studied for different conditions of thermal cycling and TMF to compare and analyze the importance and severity of thermal and mechanical loadings.

1. Thermal cycling

To investigate the role of maximum temperature on the coating microstructure, thermal cycling was carried out at the SNECMA facility using three maximum temperatures of 1373 K, 1423 K, and 1448 K (1100 °C, 1150 °C, and 1175 °C) and holding time of 45 minutes. An automatic rig placed several samples in a resistive furnace at the chosen maximum temperature. Then, forced-air cooling was achieved by moving samples out of the furnace and using air nozzles leading to an average cooling rate of about 2 K s⁻¹ (Figure 1(a)).

The influence of thermal cycling frequency was studied by comparing three holding times of 45, 15, and 5 minutes at 1373 K (1100 °C). For the holding times of 45 and 15 minutes two different resistive furnaces were used, respectively, that of SNECMA and that of MINES ParisTech—Centre des Matériaux. For the holding time of 5 minutes at 1373 K (1100 °C) a lamp furnace was used at MINES ParisTech—Centre des Matériaux: each thermal cycle was carried out in air and included heating from 373 K (100 °C) to the maximum temperature with the heating rate of 5 K s⁻¹, holding at the maximum temperature and, finally, cooling to 373 K (100 °C) with the rate of 5 K s⁻¹ using air nozzles (Figure 1(a)). It is worth noting that for the resistive furnaces the first part of the cooling, roughly down to 673 K (400 °C), was achieved with a cooling rate of about 5 K s⁻¹ (identical to that in the lamp furnace) and only further cooling, from 673 K to 373 K (400 °C to 100 °C), was slower (Figure 1(a)).

Additionally, interrupted tests were carried out for thermal cycling: after a pre-defined number of cycles, samples were cut and observed in light optical microscope. The remaining part of the sample was then reused in the cyclic procedure.

2. Thermo-mechanical fatigue

The TMF tests were performed using an Instron testing machine equipped with a lamp furnace enabling heating and cooling rate at 5 K s⁻¹ as described above.^[9,15] The maximum temperature of 1373 K (1100 °C) with holding time of 5 minutes was used. In-phase (IP) and out-of-phase (OP) tests were performed; a tensile or compressive stress, respectively was applied in such a way that the maximum absolute stress was reached at the same time as the maximum temperature, then the stress was released linearly to zero when the temperature of 373 K (100 °C) was reached (Figures 1(b) and (c)).

The TMF resulted in macroscopic creep of the substrate. The evolution of the absolute plastic strain, measured using the crosshead displacement, is shown in Figure 2. There is no significant difference between IP or OP tests in terms of the absolute plastic strain evolution.

Table I. Chemical Composition of Single-Crystal Superalloy AM1 Used in the Current Study (Weight Percent)

	Co	Cr	Mo	W	Ta	Al	Ti	C	Fe	S	Ni
Min	6	7	1.8	5	7.5	5.1	1				bal.
Max	7	8	2.2	6	8.5	5.5	1.4	0.01	0.2	0.2 ppm	bal.

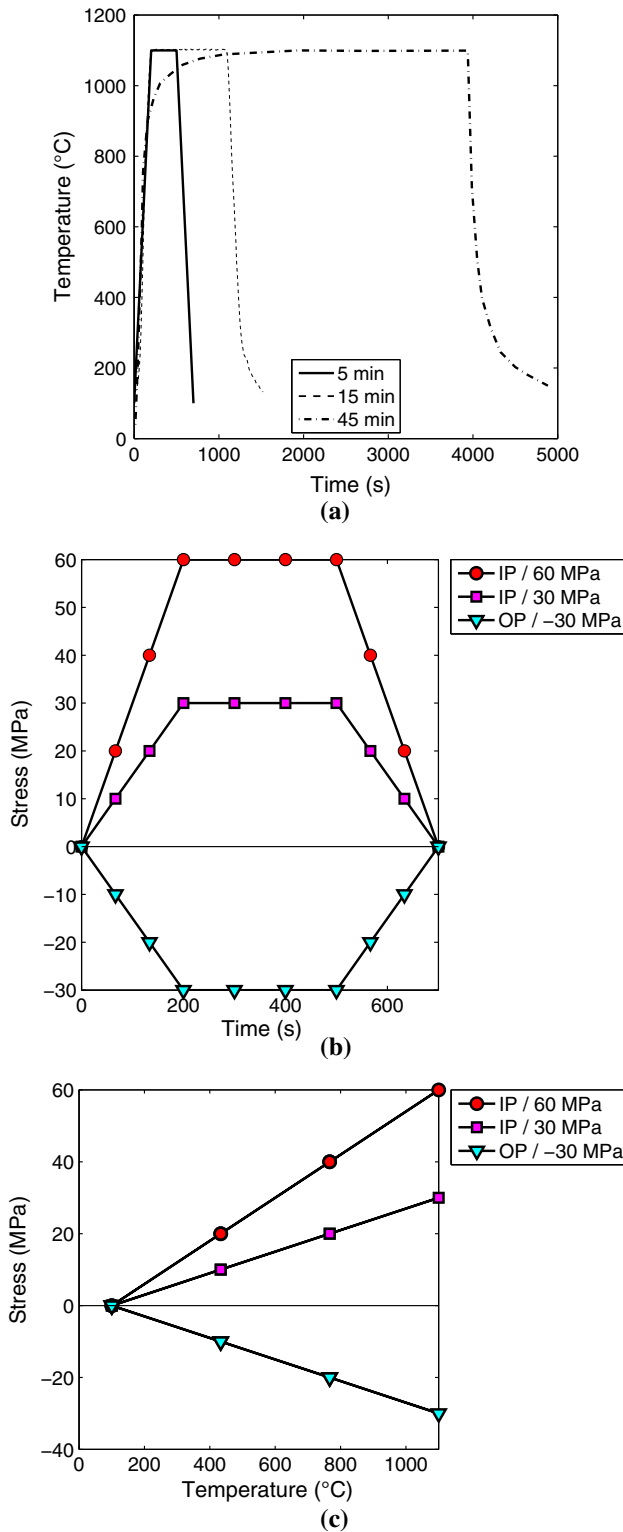


Fig. 1—Thermo-mechanical conditions used: (a) thermal cycle with holding times of 5, 15, and 45 min (from Ref. [9]), and applied stress evolutions as a function of time (b), and of temperature (c).

Nevertheless, creep rate is drastically increased when the applied stress increases from 30 to 60 MPa.

All conditions used for thermal cycling and TMF are summarized in Table II.

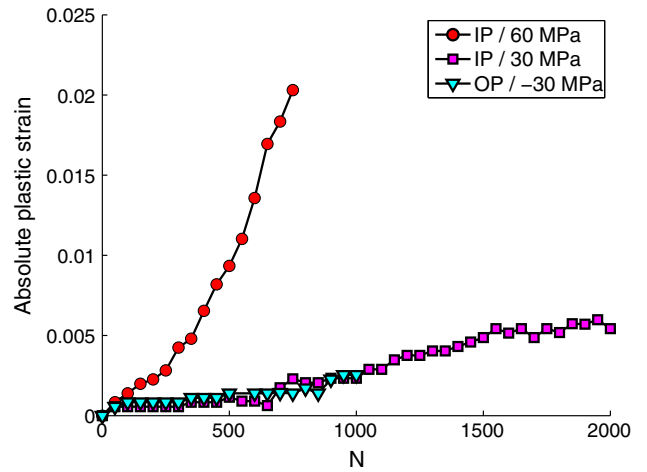


Fig. 2—Variation of the absolute plastic strain with the number of TMF cycles.

Table II. Parameters of Thermal Cycling and TMF Used in the Experimental Study

Number of Specimen Tested [Number of Cuts]	Dwell Time at T_{max} (min)	T_{max} [K (°C)]	Applied Stress (MPa)
3 [18]	5	1373 (1100)	0
4 [4]			30
2 [2]			60
2 [2]	15	1373 (1100)	-30
2 [14]			0
2 [12]			45
2 [12]	45	1423 (1150)	
2 [12]		1448 (1175)	

The “number of cuts” corresponds to the total number of samples prepared for cross-sectional analysis for both interrupted thermal cycling and final observation of TMF tests (e.g., 6 interruptions for 2 samples have led to 12 cuts and analysis for thermal cycling; for TMF only final observation is possible).

C. Sample Geometry

Different sample geometries were used depending on test type. For thermal cycling with holding time of 45 minutes at maximum temperature and without applied stress, plain cylindrical samples (40 mm in length and 7 mm in diameter) were used whereas hollow cylindrical samples (25 mm in length and 11 mm in external diameter with a wall thickness of 1 mm) were manufactured for holding times of 5 and 15 minutes to minimize thermal gradients.

For TMF a hollow cylindrical sample was optimized based on a specific geometry designed previously^[15]: overall dimensions were reduced leading to an external diameter of 7.8 mm and a wall thickness of 0.8 mm, see Figure 3.

All specimens were machined in such a way that $\langle 001 \rangle$ substrate crystallographic direction was parallel to the loading direction. The misorientation between $\langle 001 \rangle$ direction and loading direction was within 10 deg.

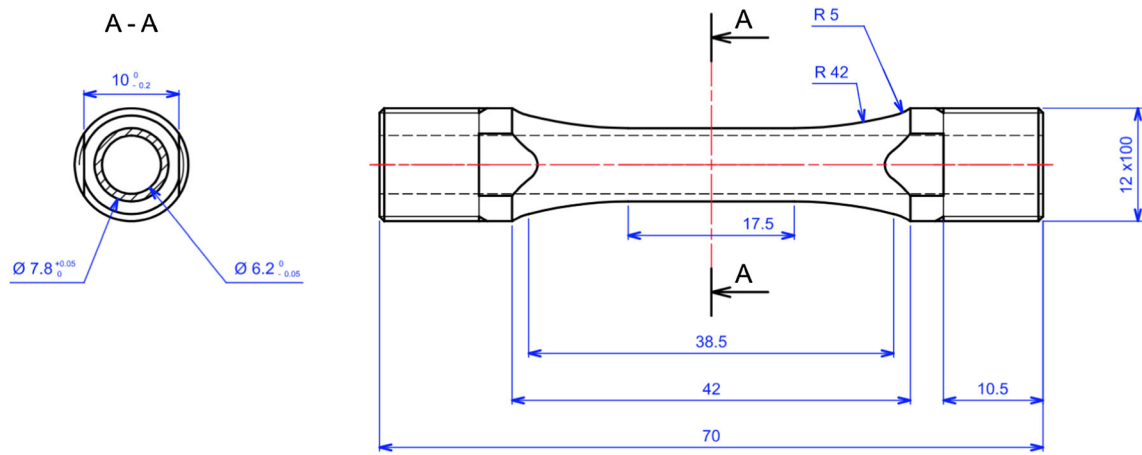


Fig. 3—Sample geometry for TMF (dimensions are given in mm).

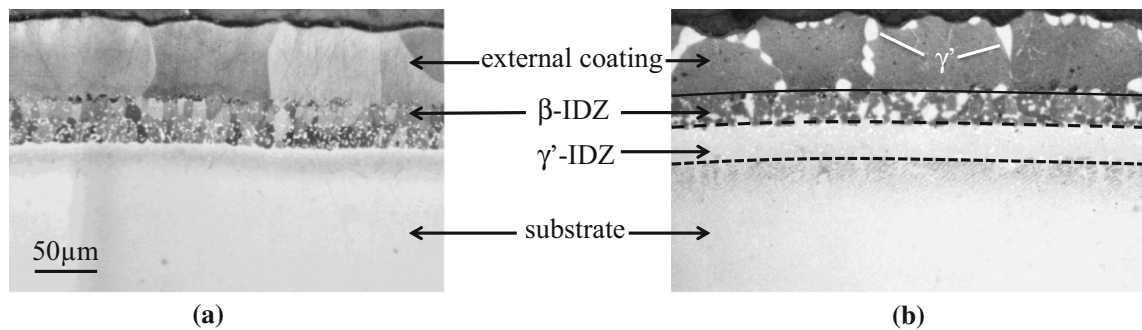


Fig. 4—Coating microstructure (a) in initial state and (b) after 100 cycles of thermal cycling with maximum temperature of 1423 K (1150 °C) and holding time of 45 min. The initial surface of the substrate is assumed to correspond to remaining alumina grit particles and is used as a reference line; this reference line is shown as a continuous line located at the external coating/ β -IDZ interface (b); the position of β -IDZ/ γ -IDZ interface is a large dashed line and the position of γ -IDZ/substrate interface is a thin dashed line.

D. Microstructure Analysis

Standard metallographic preparation including surface polishing to mirror-like quality and etching using Kalling's solution was done for all samples prior to light microscope observation.

1. Initial coating microstructure

The initial coating microstructure before thermal cycling and TMF is shown in Figure 4(a). Two different layers were observed: the outer zone referred to as external coating consisted of β -(Ni,Pt)Al grains^[31,32] and an interdiffusion zone (IDZ) was observed between the external coating and superalloy substrate. IDZ contained (Cr,W)-rich particles (topologically close-packed (TCP) phases) embedded in β -(Ni,Pt)Al grains.^[7,33,34] A line of alumina grit particles was observed as well. These alumina particles were introduced during the grit blasting process and were used to increase the surface roughness of the superalloy substrate to improve coating adherence. It will be used as a reference line to quantify coating microstructure evolution.

2. General observations after thermal cycling

After thermal cycling, a thermally grown aluminum oxide (TGO) develops onto the coating surface and

β -(Ni,Pt)Al transforms partially into γ' -Ni₃Al phase within the external layer, see Figure 4(b), in agreement with previous literature results obtained for similar coatings and conditions.^[10,11,18] Moreover, the IDZ splits into two distinct layers. The first one, called hereafter β -IDZ, consists of β -(Ni,Pt)Al grains (inherited from the initial IDZ), γ' -Ni₃Al, and TCP phases. The second one, called hereafter γ' -IDZ, develops by transformation of the β -IDZ into γ' -Ni₃Al layer. This second layer grows at the expense of both β -IDZ and the substrate.^[7]

To facilitate the layers and phase designation, an example of electron probe micro-analysis (EPMA) measurement is shown in Figure 5 for a sample after 100 cycles of thermal cycling with maximum temperature of 1423 K (1150 °C) and holding time of 45 min. The concentration profile suggests first a region of γ' -Ni₃Al phase located at initial β -(Ni,Pt)Al grain boundary, then homogeneous β -(Ni,Pt)Al phase region is observed until the line of alumina grit particles is reached. β -(Ni,Pt)Al phase is still observed with no specific variation in chemical composition between alumina particles and the substrate. Then going deeper to the substrate, a region with γ' -Ni₃Al composition (taking into

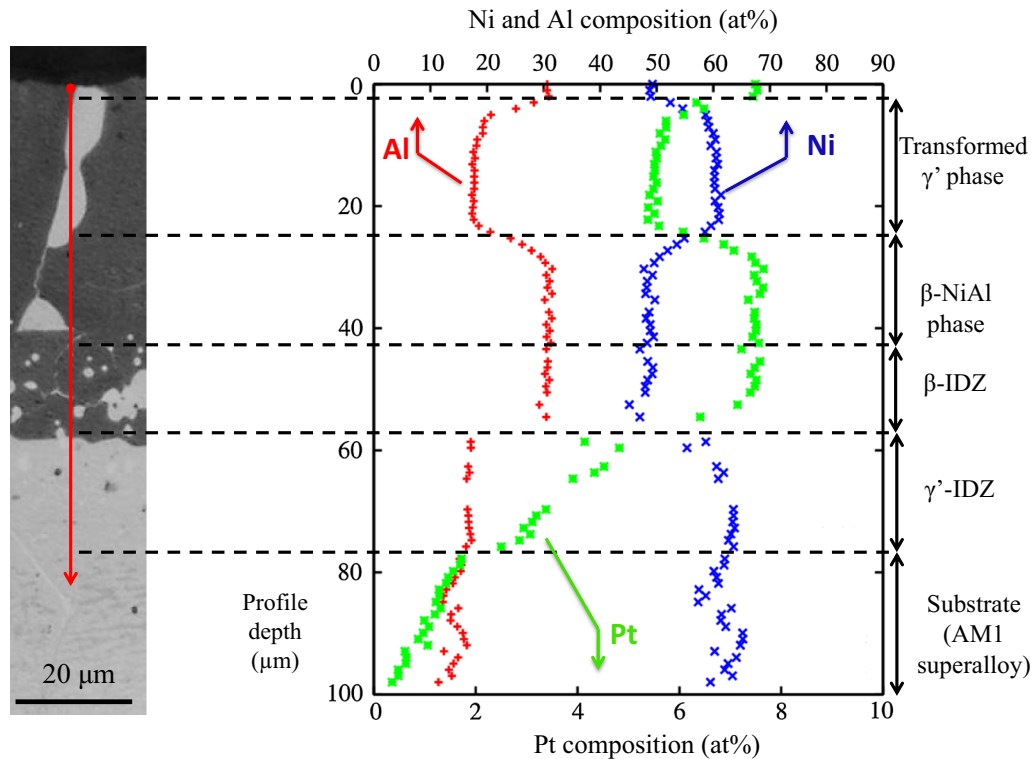


Fig. 5—Concentration profiles for Al, Pt, and Ni (at. pct) as obtained by EPMA for a sample after 100 cycles of thermal cycling with maximum temperature of 1423 K (1150 °C) and holding time of 45 min.

account other alloying elements of the superalloy) with constant Ni and Al concentration is observed, and finally γ - γ' region of Ni-based superalloy substrate is reached.

E. Image Analysis

A quantitative study of coating microstructure evolution was based on image analysis of micrographs obtained by light optical microscopy. First, the cross section is reconstructed stitching together overlapped microscope images. Secondly, a sequential process is performed to determine the location of coating layers, according to a global analysis of the cross-sectional geometry; layer thicknesses, surface and interfaces morphology, as well as phase surface fractions are determined.

1. Cross-section reconstruction

Several optical images are acquired and stitched together using DoubleTake[®] software, which applies an automatic Gaussian average at the stitched interfaces to remove any light variations. This set of contiguous images stitched together is the input for the image analysis detailed below.

A sensitivity analysis showed that at least 15 pictures were required to obtain reliable and converged microstructural features (roughness, layer thicknesses,...), leading to a final cross section spanned over at least

2 mm in width that corresponds to an arc length over 3 mm of a cylindrical sample.

2. Image processing

The image processing is based on the sequential analysis of the reconstructed cross section carried out using Matlab[®] software; each step is mainly based on gray-level analysis and is detailed in [Appendix](#).

The main idea is to use the cylindrical geometry of the cross section to determine a global reference system. Based on this reference system, the mean position of the interface between each layer (external coating, β -IDZ, γ' -IDZ, and substrate) can be determined. Final analysis consists in measurement of layer thicknesses, roughness, and phase surface fractions.

The image processing is carried out according to the following procedure:

1. Determination of the coating-free surface;
2. Determination of the β -IDZ/ γ' -IDZ interface;
3. Determination of the initial surface of the substrate using alumina grit particles;
4. Determination of the geometrical center of the cross section: the line of alumina grit particles is approximated by a circular segment and the corresponding center and radius are determined;
5. Approximation of the sample surface and β -IDZ/ γ' -IDZ interface by circular segments with the center defined in the previous step; measurement of β -IDZ thickness;

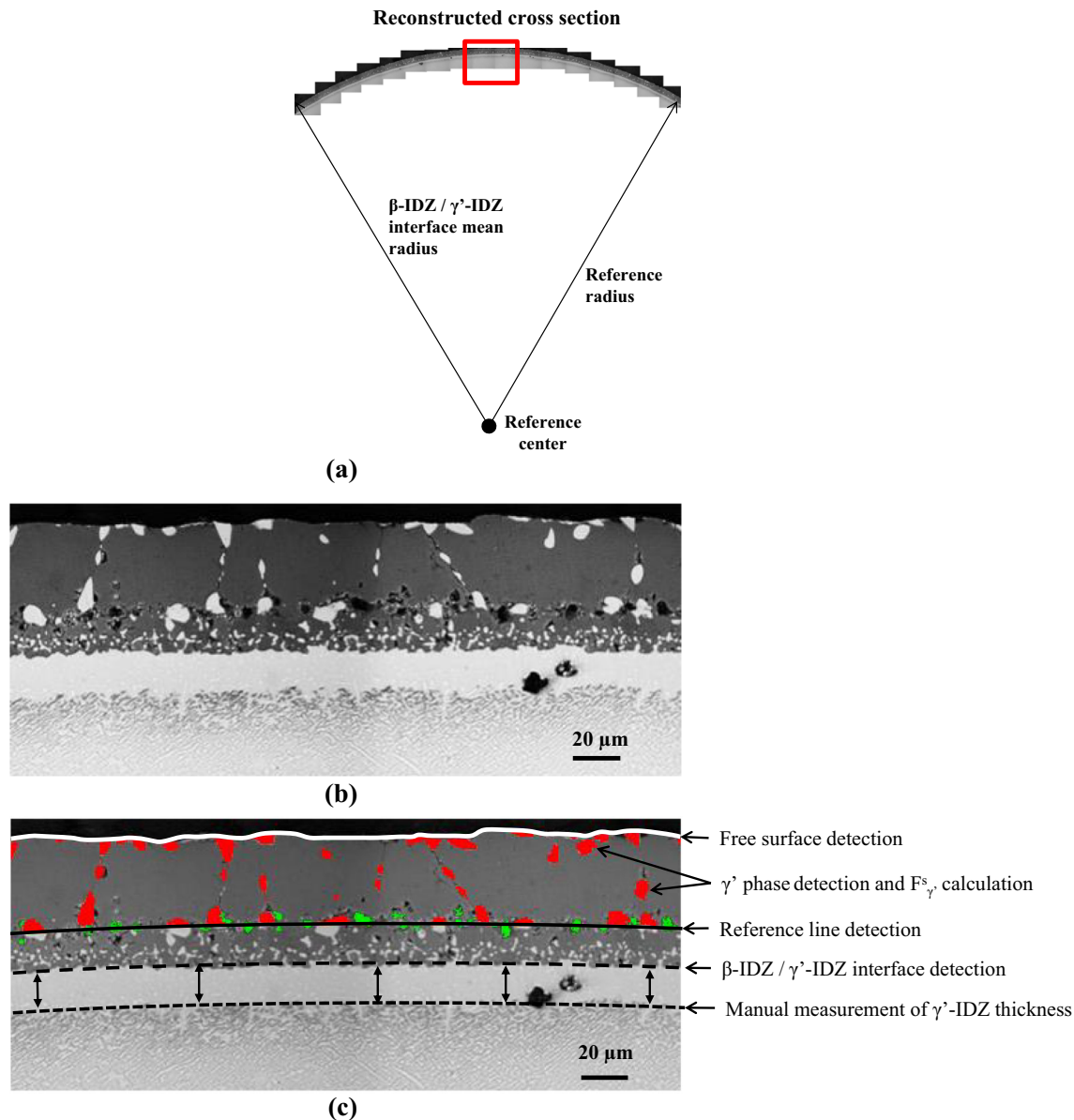


Fig. 6—Different steps of image analysis: (a) stitched image and determination of the cross-sectional geometric center by approximation of alumina grit particles by a circular segment, (b) image to be analyzed extracted from previous set of contiguous images, and (c) processed image after analysis. The sample used was subjected to 500 cycles of thermal cycling with a maximum of 1373 K (1100 °C) and holding time of 15 min.

6. Determination of the external coating location and measurement of the surface fraction of formed γ' -Ni₃Al phase, $F_{\gamma'}^s$, from initial β -(Ni,Pt)Al within the external coating;
7. Measurement of the γ' -IDZ layer thickness.

The different steps of the image analysis are summarized in Figure 6 and the detailed description is given in Appendix.

In the following, to facilitate the reading of microstructure evolution, only two adjacent micrographs are discussed for each test condition and the approximate location of the different interfaces is symbolized by partial lines located on the left-hand side of images.

III. RESULTS

A. Influence of Number of Cycles

Figure 7 illustrates the coating microstructure evolution for thermal cycling with maximum temperature of 1373 K (1100 °C) and holding time of 5 minutes for different number of cycles. One can state several evolutions as compared with the initial state (Figure 4(a)). The number and size of γ' -Ni₃Al phase precipitates formed in the external coating increase with the number of thermal cycles; γ' -Ni₃Al phase seems to nucleate at β grain boundaries, close to the free surface, and at alumina grit particles, see Figure 7(a). The increase in number of cycles, *i.e.*, increase in time

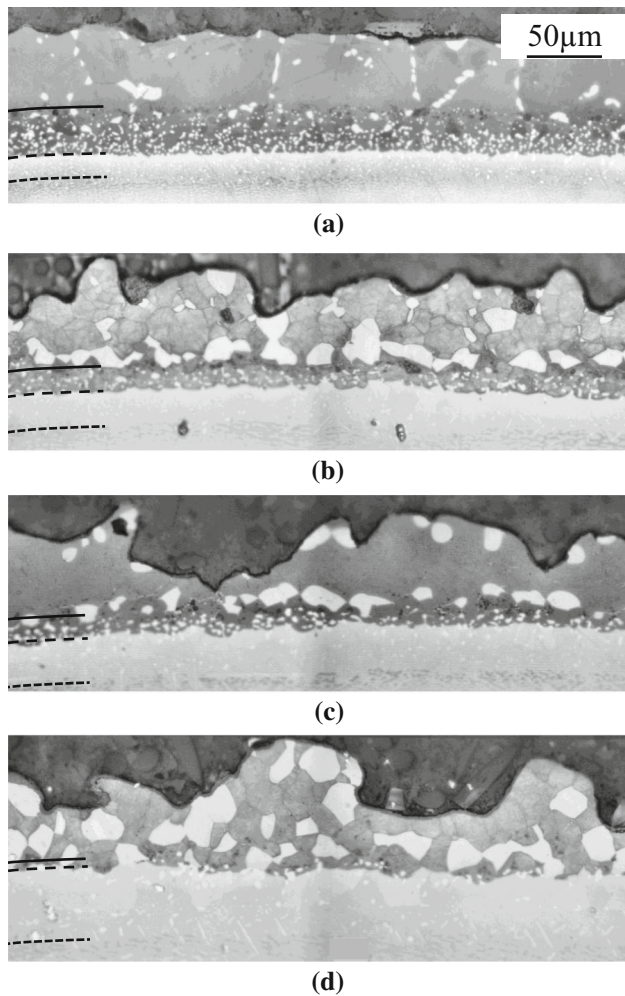


Fig. 7—Influence of the number of cycles on the coating microstructure evolution for thermal cycling with maximum temperature of 1373 K (1100 °C) and holding time of 5 min for (a) 1000, (b) 2000, (c) 3000, and (d) 5000 cycles (solid lines indicate the line of alumina grit particles corresponding to initial substrate surface position, β -IDZ/ γ' -IDZ interface and γ' -IDZ/substrate interfaces are shown using large-spaced and thin-spaced dashed lines, respectively).

accumulated at high temperature, leads to the γ' -Ni₃Al phase growth, coarsening and coalescence, resulting in a decrease in the number of γ' -Ni₃Al phase precipitates and an intricate β/γ' structure. The surface roughness, so-called “rumpling”,^[35–37] increases significantly with the number of thermal cycles.

To highlight the IDZ evolution, increased resolution images of Figures 7(a) and (c) are shown in Figure 8 (the contrast was optimized to distinguish the IDZ features).

The IDZ splits into β -IDZ and γ' -IDZ layers, as already mentioned in Figure 4(b). The β -IDZ thickness reduces with the increase in the number of thermal cycles whereas that of the γ' -IDZ increases, if one compares Figures 8(a) and (b). Some pores are also visible, but no correlation with thermal cycling was found. Similar microstructural trends are observed for all other samples after thermal cycling.

B. Influence of Maximum Temperature and Holding Time During Thermal Cycling

For the holding time of 45 minutes, three different maximum temperatures of 1373 K, 1423 K, and 1448 K (1100 °C, 1150 °C, and 1175 °C) were used for thermal cycling. When comparing the microstructures obtained after approximately 200 cycles for these three temperatures, the thermal activation of both $\beta \rightarrow \gamma'$ transformation and rumpling is highlighted by the drastic increase in γ' -Ni₃Al fraction within the external layer and increase in surface roughness, see Figure 9.

The γ' -Ni₃Al phase coarsens at initial β -(Ni,Pt)Al grain boundaries and close to the alumina grit particles. For the highest maximum temperature, a diffusion front of the γ' -IDZ layer crossed the alumina grit particles line; the initial β -IDZ layer was completely transformed into γ' -Ni₃Al phase. Moreover, the $\beta \rightarrow \gamma'$ transformation within the external coating led to a homogenous γ' -Ni₃Al layer at the TGO/coating interface and in this case, initial β -(Ni,Pt)Al phase lays between two rather continuous γ' -Ni₃Al layers.

Lastly, using almost the same time accumulated at 1373 K (1100 °C) for holding times of 45 minutes (Figure 9(a) corresponds to $45 \times 240 = 10,800$ minutes at 1373 K) and 5 minutes (Figure 7(b) corresponds to $5 \times 2000 = 10,000$ minutes at 1373 K), it can be derived that a shorter dwell at maximum temperature—*i.e.*, a higher cycling frequency—leads to an increase in both roughness and $\beta \rightarrow \gamma'$ phase transformation rate within the external coating.

C. Influence of Applied Stress During Thermal Cycling

The coating microstructure after thermal cycling with maximum temperature of 1373 K (1100 °C) and holding time of 5 minutes with applied stress is shown in Figure 10. The number of cycles is chosen equal or close to 1000 to reveal the influence of applied stress in comparison with the same thermal cycling conditions without applied stress, see Figure 7(a).

First, the roughness increases whatever the sign of applied stress. However, the coarsening of isolated γ' -Ni₃Al phase at initial β -(Ni,Pt)Al grain boundaries and close to the alumina grit particle line is seen to be more pronounced, when a stress is applied, as compared with the same thermal cycling conditions without applied stress, see Figures 10 and 7(a). Moreover, for thermal cycling without applied stress, γ' -Ni₃Al phase is spread through the whole external coating at β -(Ni,Pt)Al grain boundaries and within β grains (Figure 7(a)). Nevertheless, only γ' -Ni₃Al phase located at β -(Ni,Pt)Al grain boundaries coarsens and no intragranular γ' -Ni₃Al phase can be observed, when a stress is applied. This point is also consistent with the observation made after a higher number of cycles for thermal cycling without applied stress, see Figures 7(c) and (d), as well as for a higher maximum temperature, see Figure 9(b).

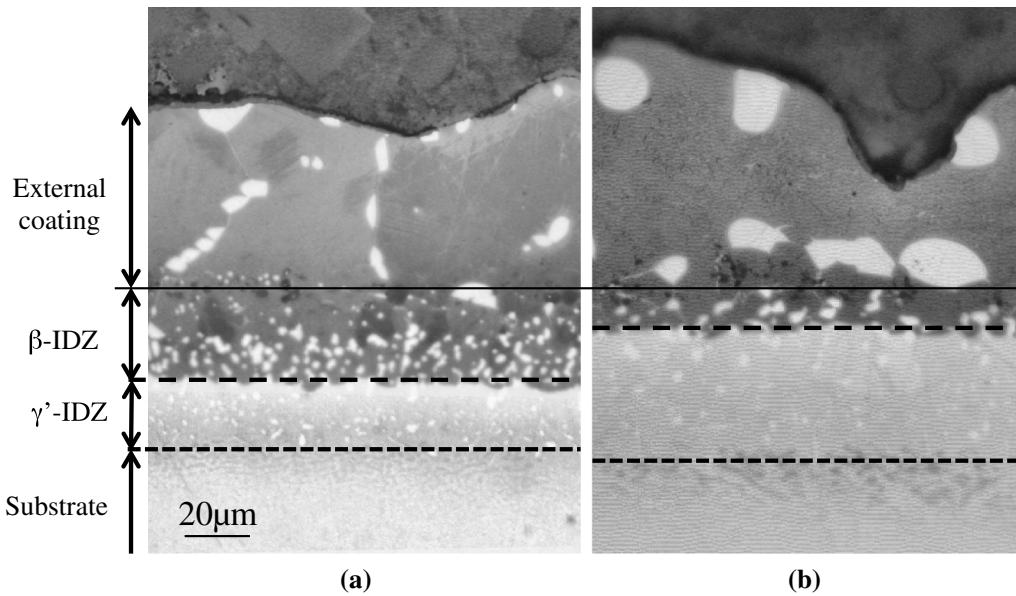


Fig. 8—Influence of the number of cycles on the coating microstructure evolution for thermal cycling with maximum temperature of 1373 K (1100 °C) and holding time of 5 min for (a) 1000, and (b) 3000 cycles ((a) is enlarged Figs. 7(a) and (b) is enlarged Fig. 7(c)).

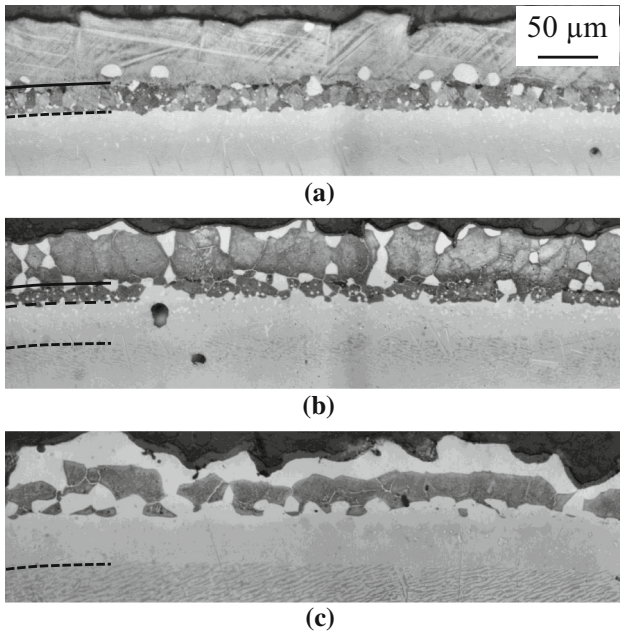


Fig. 9—Coating microstructure after thermal cycling with the holding time of 45 minutes for (a) 240 cycles and maximum temperature of 1373 K (1100 °C), (b) 200 cycles and maximum temperature of 1423 K (1150 °C), and (c) 200 cycles and maximum temperature of 1448 K (1175 °C) (solid lines indicate the line of alumina grit particles corresponding to initial substrate surface position, β -IDZ/ γ' -IDZ interface, and γ' -IDZ/substrate interfaces are shown using large-spaced and thin-spaced dashed lines, respectively).

IV. DISCUSSION

A. $\beta \rightarrow \gamma'$ Transformation

To quantify the influence of holding time at maximum temperature on coating microstructure evolution, the obtained $F_s^{\gamma'}$ values are plotted as a function of the time accumulated at maximum temperature (Figure 11). One

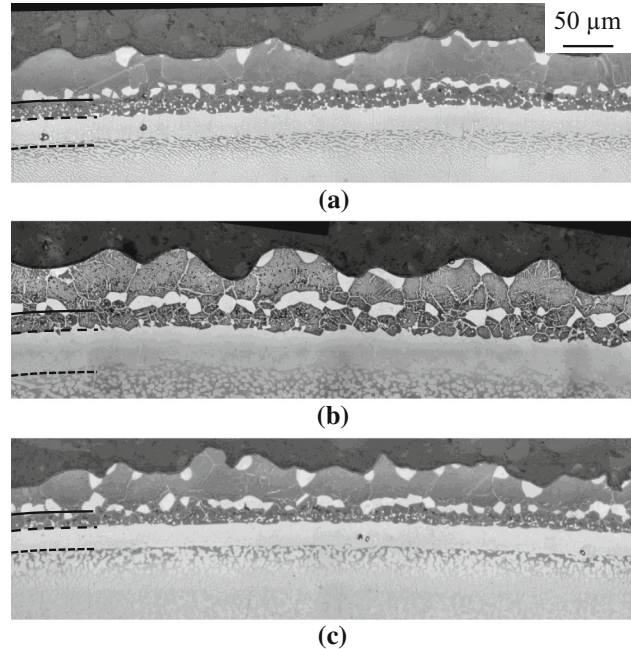


Fig. 10—Coating microstructure after TMF: thermal cycling with maximum temperature of 1373 K (1100 °C) and holding time of 5 min for (a) out-of-phase (OP) test with $\sigma = -30$ MPa and 1000 cycles, (b) in-phase (IP) test with $\sigma = 30$ MPa and 1000 cycles, and (c) in-phase (IP) test with $\sigma = 60$ MPa and 750 cycles (σ is applied stress).

can see that $F_s^{\gamma'}$ increases monotonously with time accumulated at maximum temperature, see Figure 11(a). Moreover, the evolution of $F_s^{\gamma'}$ is thermally activated. An increase in the $\beta \rightarrow \gamma'$ transformation rate is observed for the holding time of 5 minutes at 1373 K (1100 °C), as compared with a holding time of 15 and 45 minutes at the same maximum temperature, see Figure 11(a). It is worth noting that, even if holding time of 5 minutes was

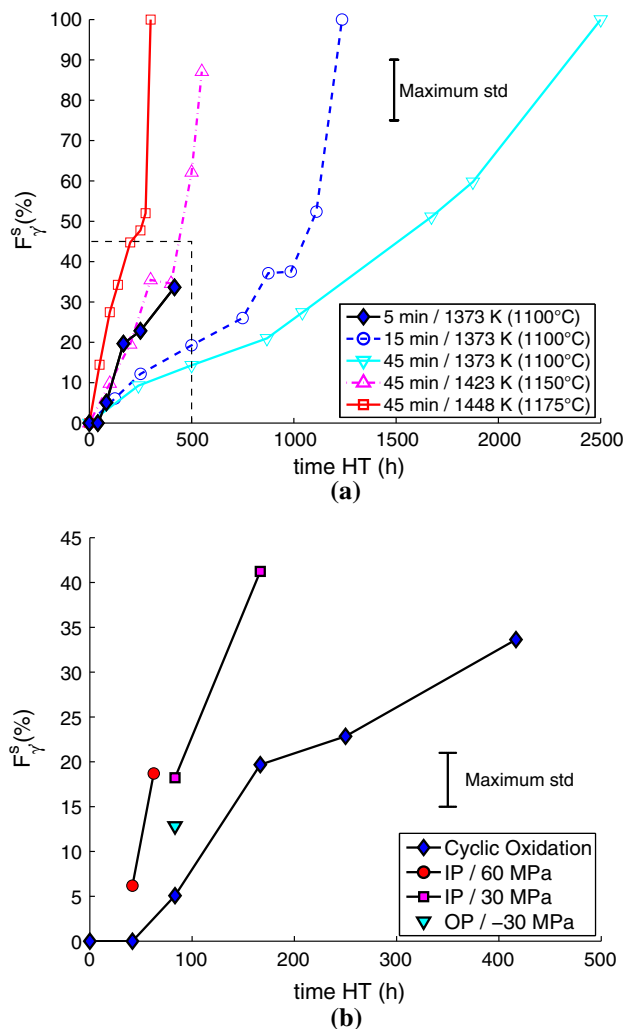


Fig. 11—Transformed surface fraction of the external coating from β to γ' for (a) different maximum temperatures and holding times and (b) for holding time of 5 min at 1373 K (1100 °C) and different applied stresses (dashed line in (a) corresponds to range plot of (b)).

performed with lamp furnace and a higher cooling rate than for 15 and 45 minutes holding time performed with resistive furnace, the increase in the rate of transformation is clearly evidenced when increasing the number of thermal cycles for the same cumulated time at 1373 K (1100 °C).

TMF leads to a faster increase in $F_s^{\gamma'}$ when compared with thermal cycling without applied stress, irrespective of the sign of the applied stress (Figure 11(b)).

An increased rate of the $\beta \rightarrow \gamma'$ phase transformation due to the maximum temperature increase from 1373 K to 1448 K (1100 °C to 1175 °C) is of the same order of magnitude as that due to the applied stress increase from 0 to 30 MPa at 1373 K (1100 °C) (e.g., compare $F_s^{\gamma'}$ obtained for in-phase test with applied stress of 30 MPa and holding time of 5 minutes at 1373 K (1100 °C) and that obtained after thermal cycling with holding time of 45 minutes at 1448 K (1175 °C) without applied stress). These measurements, together with morphology and phase location discussed previously, suggest that the

applied stress has a similar accelerating effect on $\beta \rightarrow \gamma'$ transformation rate as the increase in temperature.

B. IDZ Evolution

The thickness of both β -IDZ and γ' -IDZ layers were investigated for thermal cycling with maximum temperature of 1373 K (1100 °C) and holding time of 5 minutes without applied stress, see Figure 12(a). For more than 500 cycles, the thickness of β -IDZ layer reduced monotonously as a function of the time spent at maximum temperature whereas that of γ' -IDZ layer increased, and the sum of thicknesses of both layers lead to a rather constant thickness value.

The influence of applied stress on β -IDZ and γ' -IDZ thicknesses is shown in Figure 12(b). For in-phase TMF tests, an increase in applied stress leads to a faster decrease in β -IDZ and to a faster increase in γ' -IDZ thicknesses. When out-of-phase loading is applied, it is noteworthy that the decrease in β -IDZ thickness is similar to that during in-phase loading, whereas increase in γ' -IDZ thickness is almost equal to that during thermal cycling without applied stress. These observations are consistent with the analysis of $\beta \rightarrow \gamma'$ transformation for in- and out-of-phase TMF.

C. Processes Controlling the Coating Microstructure Evolution

The microstructure observations for TMF showed that both the external coating and IDZ are sensitive to the maximum temperature, the holding time at maximum temperature, and the applied stress. First, the $\beta \rightarrow \gamma'$ phase transformation is mainly governed by diffusion and thus is thermally activated and formed γ' phase fraction increases with time spent at high temperature. This statement is valid for both γ' -Ni₃Al phase formation within the external coating and for the growth of the γ' -IDZ layer from the substrate to the external coating. The recession of the β -IDZ is also a consequence of cross diffusion of Ni to the surface and Al to the substrate superalloy.

It was shown that an applied stress during thermal cycling leads to a similar increase in γ' phase fraction within the external coating as that when the temperature or holding time are increased. For instance, the increase in γ' surface fraction observed for a temperature increase from 1423 K to 1473 K (1150 °C to 1175 °C), see Figure 11(a), is almost the same as that for an applied stress of 30 MPa compared with pure thermal cycling, see Figure 11(b).

The influence of holding time is shown for 1373 K (1100 °C) using different holding times of 5, 15, and 45 minutes. This observation suggests an important influence of the number of thermal cycles on coating microstructure evolution already mentioned by several authors^[9,37] and could be related to stress-diffusion coupling. Indeed, an increase in the number of thermal cycles leads to an increase in plasticity due to the mismatch of coefficient of thermal expansion between different layers.

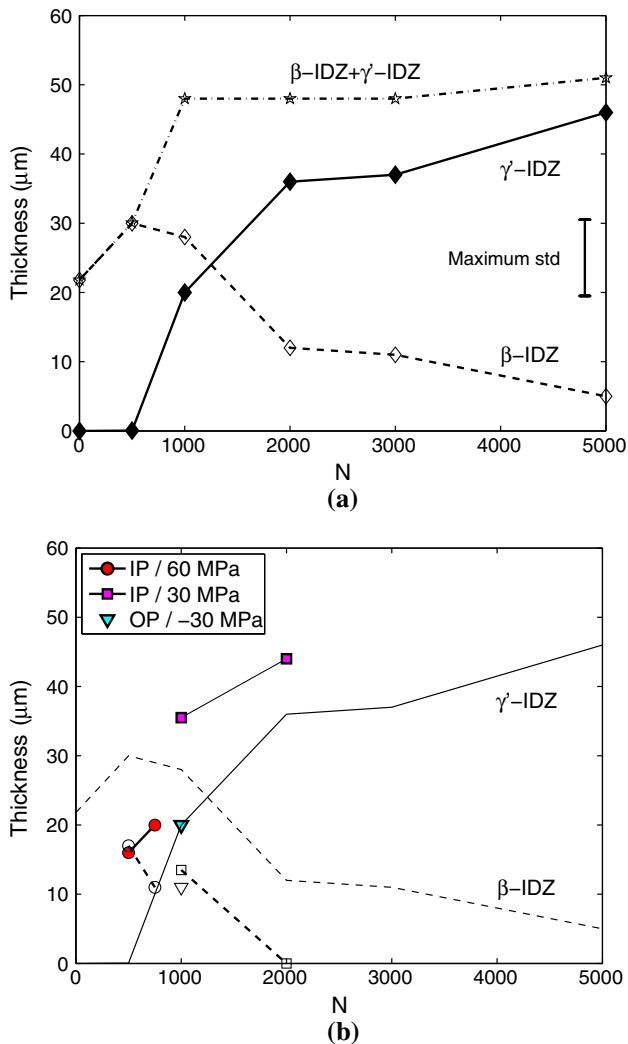


Fig. 12—Thickness evolution of the (a) β -IDZ (open symbols) and γ' -IDZ (solid symbols) layers and sum of β -IDZ and γ' -IDZ layer thicknesses as a function of the number of cycles N for thermal cycling at a maximum temperature of 1373 K (1100 °C) and holding time of 5 min and (b) β -IDZ (open symbols) and γ' -IDZ (solid symbols) for different TMF in-phase (IP) and out-of-phase (OP) conditions (the evolutions for thermal cycling are used as a reference in graph (b) and represented by solid lines).

The sensitivity of γ' -IDZ thickness increases to applied stress (hence, the decrease of β -IDZ) is analogous to that observed for γ' -Ni₃Al formation within the external coating. The stress-diffusion coupling observed for the IDZ is probably similar to other observations made for Ni-based single-crystal superalloys with or without coating when creep-fatigue interactions dominate, leading to an increase in phase transformation rate (e.g., rafting).^[17,30,38] Thus, the proposed description of IDZ evolution showed that during thermal cycling, even for a low level of applied stress at maximum temperature, in the range [−30; +60 MPa], a significant decrease in the load bearing section or at least a drastic evolution of the IDZ should

be accounted for. Due to high temperature, these low levels of stress led to considerable level of plasticity due to typical creep-fatigue condition during thermal cycling, see Figure 2.

Moreover, the growth of γ' -Ni₃Al phase within the external coating is either located at initial β -(Ni,Pt)Al grain boundaries or within β grains for thermal cycling. When stress is applied, γ' -Ni₃Al phase coarsening accelerates at both oxide/coating and coating/IDZ interfaces, whereas volume fraction of γ' -Ni₃Al phases located within β -(Ni,Pt)Al grains decreases. For a temperature increase, the γ' -Ni₃Al phase coarsening seems to be independent of γ' -Ni₃Al phase location among β -(Ni,Pt)Al phase grain boundaries, oxide/external coating, or external coating/IDZ interfaces. This point evidences that stress/strain gradients induced by grain boundaries within the external coating layer^[34] and multi-layered structure of the coating/substrate^[39] have a key role in stress-diffusion coupling and subsequent phase transformation.

All these observations seem to be related to a strong mechanical-diffusion coupling without any evidence of damage-like coating cracking as previously reported for Ni-Al coating.^[9,18]

Lastly, unusual apparent symmetry of tension/compression effect at maximum temperature requires additional detailed analysis, whereas most authors only consider stress-diffusion coupling for positive stress or either positive hydrostatic pressure.^[40] It could be related to the influence of dislocation density^[41] and plastic strain gradient at the level of grain boundaries and interfaces and should be deeply analyzed.

V. SUMMARY

It has been shown that parameters of TMF: maximum temperature, holding time at maximum temperature, as well as applied stress had a strong impact on microstructure evolution of the platinum-modified nickel-aluminide coating.

An increase in the number of thermal cycles with constant maximum temperature and without applied stress leads to a growth of γ' -Ni₃Al precipitates in the external coating. The IDZ splits into β -IDZ and γ' -IDZ layers with subsequent β -IDZ thickness reduction and γ' -IDZ thickness increase, respectively. On the other hand, rumpling increases significantly.

Thermal activation of both $\beta \rightarrow \gamma'$ transformation and rumpling are shown, respectively by the increase in γ' -Ni₃Al fraction within the external layer and in surface roughness, when the maximum temperature during thermal cycling is increased.

When a stress is applied, coarsening of isolated γ' -Ni₃Al phase at initial β -(Ni,Pt)Al grain boundaries and close to the alumina grit particles line is seen to be more pronounced. Moreover, the growth of γ' -IDZ layer is also sensitive to applied stress at high temperature during thermal cycling.

ACKNOWLEDGMENTS

Vladimir Esin (Mines ParisTech) is gratefully acknowledged for his discussions and careful reading of this paper. This work was supported by SNECMA/Safran Group and the French Ministry of Transportation (Direction des Programmes de l'Aviation Civile) which are also acknowledged. The authors are grateful to SNECMA for supplying the coated superalloys and for availability of their experimental facilities.

APPENDIX: IMAGE ANALYSIS METHODOLOGY

After image stitching described above, a program has been developed using Matlab[®] software to determine geometric parameters and microstructure features. Different steps of image analysis are detailed below:

1. Determination of the coating-free surface. The gray-level gradient between the resin used for sample preparation and the coating surface defines the coating surface profile. It is obtained after segmentation, edge detection, and 2D Bresenham smoothing^[42];
2. Determination of the β -IDZ/ γ' -IDZ interface. The contrast between the β -IDZ and γ' -IDZ layers (gray vs white) defines the interface between these two layers. It is again obtained after segmentation, edge detection, and 2D Bresenham smoothing;
3. Determination of the initial surface of the substrate. The area bounded by the surface profile and the β -IDZ/ γ' -IDZ interface, *i.e.*, external coating + β -IDZ layer, is isolated. Alumina grit particles are assumed to correspond to the original sample surface. They are found through gray-level gradient analysis;
4. Determination of the geometrical center of the cross section. The center and the radius of the circle that fit best with these particles are obtained by least square method. This set of geometric parameters defines the reference line;
5. Approximation of the sample surface and β -IDZ/ γ' -IDZ interface by circular segments with the center defined in the previous step; measurement of β -IDZ thickness. Using the reference center determined above and using the same optimizing method, the radius of the circle that fits to the surface profile, and to the β -IDZ/ γ' -IDZ interface, respectively are calculated. The subtraction of the radius associated with the β -IDZ/ γ' -IDZ interface with the reference radius gives the average β -IDZ thickness;
6. Determination of the external coating location and measurement of the surface fraction of the formed γ' -Ni₃Al phase, $F_s^{\gamma'}$. The area bounded by the surface profile and the reference line, defines the external coating. The contrast between the β and γ' phases allows a direct thresholding analysis using Otsu's method^[43]; the number of pixel belonging to the γ' phases is obtained. The ratio with the total number of pixel contained in the external coating gives the surface fraction of external coating transformed into γ' phases, *i.e.*, $F_s^{\gamma'}$;
7. Measurement of the γ' -IDZ layer thickness. Finally, the γ' -IDZ layer thickness is evaluated for each cross section manually, measuring the length of segments drawn between the β -IDZ/ γ' -IDZ interface and the γ' -IDZ/substrate interface. More than 20 segments are measured for each reconstructed profile.

The different steps and features detected by the program are summarized in Figure 6(c).

REFERENCES

1. M.S. Farrell, D.H. Boone, and R. Streiff: *Surf. Coat. Technol.*, 1987, vol. 32 (1), pp. 69–84.
2. B.A. Pint, I.G. Wright, W.Y. Lee, Y. Zhang, K. Pruessner, and K.B. Alexander: *Mater. Sci. Eng. A*, 1998, vol. 245 (2), pp. 201–11.
3. J. Benoist, K.F. Badawi, A. Malié, and C. Ramade: *Surf. Coat. Technol.*, 2004, vol. 182, pp. 14–23.
4. J. Angenete and K. Stiller: *Mater. Sci. Eng. A*, 2001, vol. 316 (1), pp. 182–94.
5. J. Angenete, K. Stiller, and E. Bakchinova: *Surf. Coat. Technol.*, 2004, vol. 176 (3), pp. 272–83.
6. F. Pedraza, A.D. Kennedy, J. Kopecek, and P. Moretto: *Surf. Coat. Technol.*, 2006, vol. 200 (12), pp. 4032–39.
7. E. Basuki, A. Crosky, and B. Gleeson: *Mater. Sci. Eng. A*, 1997, vol. 224, pp. 27–32.
8. J.A. Nesbitt: *Oxid. Met.*, 1995, vol. 44 (1–2), pp. 309–38.
9. L. Rémy, A. Alam, and A. Bickard: *ASTM STP*, 2003, vol. 1428, pp. 98–111.
10. N. Vialas and D. Monceau: *Oxid. Met.*, 2006, vol. 66 (3–4), pp. 155–89.
11. H.E. Evans: *Surf. Coat. Technol.*, 2011, vol. 206, pp. 1512–21.
12. S. Darzens, D.R. Mumm, D.R. Clarke, and A.G. Evans: *Metall. Mater. Trans. A*, 2003, vol. 34A, pp. 511–22.
13. C. Guerre, L. Rémy, and R. Molins: *Mater. High Temp.*, 2003, vol. 20 (4), pp. 481–85.
14. C. Duhamel, M. Chieux, R. Molins, and L. Rémy: *Mater. High Temp.*, 2012, vol. 29 (2), pp. 136–44.
15. J.L. Malpertu and L. Rémy: *Metall. Trans. A*, 1990, vol. 21A, pp. 389–99.
16. E. Fleury and L. Rémy: *Metall. Mater. Trans. A*, 1994, vol. 25A, pp. 99–1s09.
17. J. Bressers, D.J. Arrell, K. Ostolaza, and J.L. Vallés: *Mater. Sci. Eng. A*, 1996, vol. 220 (1), pp. 147–54.
18. P. Moretto and J. Bressers: *J. Mater. Sci.*, 1996, vol. 31, pp. 4817–29.
19. T.C. Totemeier, W.F. Gale, and J.E. King: *Mater. Sci. Eng. A*, 1993, vol. A169, pp. 19–26.
20. T.C. Totemeier, W.F. Gale, and J.E. King: *Metall. Mater. Trans. A*, 1996, vol. 27A, pp. 363–69.
21. O. Franke, K. Durst, and M. Göken: *Mater. Sci. Eng. A*, 2007, vol. 467 (1), pp. 15–23.
22. P.K. Wright: *Mater. Sci. Eng. A*, 1998, vol. 245, pp. 191–200.
23. M. Bartsch, B. Baufeld, S. Dalkilic, L. Chernova, and M. Heinzelmann: *Int. J. Fatigue*, 2008, vol. 30 (2), pp. 211–18.
24. A.G. Evans, M.Y. He, A. Suzuki, M. Gigliotti, B. Hazel, and T.M. Pollock: *Acta Mater.*, 2009, vol. 57 (10), pp. 2969–83.
25. L. Rémy, C. Guerre, I. Rouzou, and R. Molins: *Oxid. Met.*, 2014, vol. 81 (1–2), pp. 3–15.
26. F. Riallant, J. Cormier, A. Longuet, X. Milhet, and J. Mendez: *Metall. Mater. Trans. A*, 2014, vol. 45A, pp. 351–60.
27. Y.H. Zhang, D.M. Knowles, and P.J. Withers: *Surf. Coat. Technol.*, 1998, vol. 107 (1), pp. 76–83.
28. R. Nützel, E. Affeldt, and M. Göken: *Int. J. Fatigue*, 2008, vol. 30 (2), pp. 313–17.
29. L. Rémy, H. Bernard, J.L. Malpertu, and F. Rezaei-Aria: in *ASTM STP 1186*, H. Sehitoglu, ed., ASTM, Pennsylvania, 1993, pp. 3–16.
30. M. Brunner, M. Bensch, R. Völkl, E. Affeldt, and U. Glatzel: *Mater. Sci. Eng. A*, 2012, vol. 550, pp. 254–62.
31. J. Benoist, K.F. Badawi, A. Malié, and C. Ramade: *Surf. Coat. Technol.*, 2004, vol. 182 (1), pp. 14–23.

32. D.K. Das: *Prog. Mater. Sci.*, 2013, vol. 58, pp. 151–82.
33. C.M.F. Rae, M.S. Hook, and R.C. Reed: *Mater. Sci. Eng. A*, 2005, vol. 396 (1), pp. 231–39.
34. V. Maurel, L. Rémy, M. Harvey, H. Tezenas du Montcel, and A. Koster: *Surf. Coat. Technol.*, 2013, vol. 215, pp. 52–61.
35. L.C. Zhang and A.H. Heuer: *Metall. Mater. Trans. A*, 2005, vol. 36A, pp. 43–53.
36. V.K. Tolpygo and D.R. Clarke: *Acta Mater.*, 2004, vol. 52 (17), pp. 5115–27.
37. V.K. Tolpygo and D.R. Clarke: *Scripta Mater.*, 2007, vol. 57 (7), pp. 563–66.
38. H.J. Kolkman: *Mater. Sci. Eng.*, 1987, vol. 89, pp. 81–91.
39. A.G. Evans, D.R. Mumm, J.W. Hutchinson, G.H. Meier, and F.S. Pettit: *Prog. Mater. Sci.*, 2001, vol. 46 (5), pp. 505–53.
40. Z. Suo, D.V. Kubair, A.G. Evans, D.R. Clarke, and V.K. Tolpygo: *Acta Mater.*, 2003, vol. 51 (4), pp. 959–74.
41. E.W. Hart: *Acta Metall.*, 1957, vol. 5, p. 597.
42. J.E. Bresenham: *IBM Syst. J.*, 1965, vol. 4 (1), pp. 25–30.
43. N. Otsu: *IEEE. Trans. Syst. Man. Cyber.*, 1979, vol. 9 (1), pp. 62–66.